Additive Manufacturing 41 (2021) 101958

Contents lists available at ScienceDirect

Additive Manufacturing

journal homepage: www.elsevier.com/locate/addma

Research Paper

# Oxidation in wire arc additive manufacturing of aluminium alloys

Tobias Hauser [a,d,*], Raven T. Reisch [b,d], Philipp P. Breese [c,d], Yogesh Nalam [d], Kaivalya S. Joshi [d], Katharina Bela [d], Tobias Kamps [d], Joerg Volpp [a], Alexander F.H. Kaplan [a]

[a] Department of Engineering Sciences and Mathematics, Luleå University of Technology, S-971 87 Luleå, Sweden
[b] Chair of Robotics, Artificial Intelligence and Real-time Systems, Technical University of Munich, D-80333 Munich, Germany
[c] Coating Technology, TU Berlin, Pascalstr. 8-9, 10587 Berlin, Germany
[d] Technology, Siemens AG, D-81739 Munich, Germany

ARTICLE INFO

*Keywords:*
Direct energy deposition
WAAM
Surface oxidation
Anomalies
In-situ monitoring

ABSTRACT

Wire Arc Additive Manufacturing is a near-net-shape machining technology that enables low-cost production of large and customised metal parts. In the present work, oxidation effects in Wire Arc Additive Manufacturing of the aluminium alloy AW4043/AlSi5(wt%) were investigated. Two main oxidation effects, the surface oxidation on aluminium parts and the oxidation anomalies in aluminium parts were observed and analysed. The surface oxidation on aluminium parts changed its colour during Wire Arc Additive Manufacturing from transparent to white. In the present work, it was shown by high-speed imaging that this change in the surface oxidation took place in the process zone, which was covered by inert gas. Since the white surface oxidation formed in an inert gas atmosphere, it was found that the arc interacts with the existing amorphous oxide layer of the previously deposited layer and turns it into a white duplex (crystalline and amorphous) oxide layer. In addition to the analysis of the white surface oxidation, oxidation anomalies, which occur at low shielding from the environment, were investigated. It was shown by physical experiments and Computational Fluid Dynamics simulations, that these oxidation anomalies occur at inadequate gas flow rates, too big nozzle-to-work distances, process modes with too high heat input, or too high wire feed rates. Finally, a monitoring method based on light emission spectroscopy was used to detect oxidation anomalies as they create peaks in the spectral emission when they occur.

## 1. Introduction

### 1.1. Wire arc additive manufacturing of aluminium alloys

Aluminium alloys are widely used in different industrial fields such as aerospace, ship building, and automotive industries because of their light weight and high corrosion resistance [1,2]. Besides ultra-pure aluminium, various aluminium alloys with the alloying elements copper, silicon, magnesium, zinc, and manganese are used [3,4]. Aluminium - silicon (Si) alloys are commonly used for welding applications, which makes them promising alloys for Wire Arc Additive Manufacturing (WAAM). WAAM is a Direct Energy Deposition process, which is focused on cost-effective production of large components due to its high deposition rates compared to other Additive Manufacturing technologies e.g. laser-based Additive Manufacturing processes [5]. WAAM processes are mainly based on Gas Metal Arc Welding (GMAW), which has a high energy input into the base material due to the high temperatures of the arc reaching up to 10,000 K [6]. As the energy input is that high, the temperature balance is of high importance, especially for WAAM of aluminium alloys, as Hauser et al. have proven by the detection of geometric deviations due to excessive process temperatures [7]. One of the most promising GMAW processes in terms of temperature balance is the Cold Metal Transfer (CMT) process, which allows a reduced energy input compared to other GMAW processes [8–10]. During the CMT process, the wire is fed into the process zone by a push and pull movement [9,11,12]. In a CMT cycle, a pulse of defined duration melts the end of the wire and feeds the wire until the wire tip touches the melt pool, creating a short circuit and arc extinction [9]. Thereupon, the wire is mechanically pulled back, separating the wire from the melt pool, and the CMT cycle restarts [9].

* Correspondence to: Luleå Tekniska Universitet, 971 87 Luleå, Sweden.
*E-mail addresses:* tobias.hauser@ltu.se (T. Hauser), raven.reisch@tum.de (R.T. Reisch), philipp.breese@siemens.com (P.P. Breese), yogesh.nalam@rwth-aachen.de (Y. Nalam), kaivalya.joshi@rwth-aachen.de (K.S. Joshi), katharina.bela@siemens.com (K. Bela), tobias.kamps@siemens.com (T. Kamps), jorg.volpp@ltu.se (J. Volpp), Alexander.Kaplan@ltu.se (A.F.H. Kaplan).

https://doi.org/10.1016/j.addma.2021.101958
Received 30 December 2020; Received in revised form 4 March 2021; Accepted 9 March 2021
Available online 19 March 2021

### 1.2. Surface oxidation in WAAM of aluminium alloys

Oxidation is one of the main problems faced in WAAM of aluminium alloys, but it has received less attention than pores and crack defects. However, oxidation also affects defects such as pores and cracks due to the remelting processes in Additive Manufacturing, whereby the oxides of the surface oxidation enter the melt pool and act as impurities. Oxidation is thus an important defect that must be addressed. Aluminium is a highly reactive element and has a strong binding affinity for oxygen. When aluminium reacts with oxygen, mainly $Al_2O_3$ is formed which has a high hardness and a whitish surface [13]. Aluminium oxides have a melting temperature at 2050 °C, which is 1390 K higher than the melting temperature of aluminium (660 °C), and a thermal conductivity of 12 W/mK to 38.5 W/mK, which is about ten times lower than that of aluminium (237 W/mK). In the WAAM process, based on GMAW, aluminium oxides form by plasma induced thermal chemical reactions [24]. The aluminium oxides consist mainly of α-$Al_2O_3$ and γ-$Al_2O_3$ [14]. At relatively low temperatures (below 300 °C) the surface oxidation is a continuous amorphous film that thickens due to diffusion effects [15]. At high temperatures, the diffusion effects increase, and duplex oxide layers containing both crystalline and amorphous oxides develop [15]. If reactive alloying elements such as magnesium and lithium are present, selective oxidation occurs, which leads to the formation of thick, friable, crystalline oxide layers [15]. At ambient temperatures, the surface oxidation film immediately grows to a thickness of a few micrometres and increases to twice or triple this thickness over a few days [15]. At a temperature of 400–650 °C a different growth is visible, because the aluminium oxides change from an amorphous structure to a compact crystalline structure, which slows down the growth [15,16]. Due to the different oxidation phenomena at different temperatures showing different characteristics, it is an important issue for WAAM as the temperatures can vary greatly depending on the process mode, wire feed rate, voltage and current. Therefore, in this work, the impact of oxidation in WAAM was further investigated to explain in more detail how the formation of the oxides happens.

### 1.3. Oxidation anomalies in WAAM of aluminium alloys

One of the big challenges in WAAM using aluminium is the occurrence of anomalies such as pores, cracks, and oxidation. Process parameters such as voltage, current, wire feed speed, interpass temperature, shielding gas flow and many others can influence oxidation effects. In particular, the influence of the gas flow from the nozzle into the processing zone is much more complex than is often assumed, since an increase of the gas flow rate does not necessarily lead to a better shielding effect [17]. On the contrary, an increase of gas velocity can increase the mixing of the shielding gas flow with the atmosphere [18]. As heated aluminium comes into contact with the ambient air and the oxygen it contains, strong aluminium oxidation occurs as an exothermic redox reaction [19]. If a high proportion of ambient air gets in contact with molten aluminium, uneven accumulations of material with a rough and whitish surface occur, which are defined as oxidation anomalies in this paper. These oxidation anomalies change the characteristics of the material, such as the mechanical properties, which affects the part quality. Therefore, the occurrence of these oxidation anomalies must be avoided. In this work, physical experiments and Computational Fluid Dynamics simulations were used to investigate how these oxidation anomalies are affected by the gas flow rate, the nozzle-to-work distance, the process mode, and the wire feed rate.

### 1.4. In-situ light emission spectroscopy in WAAM

Different researchers have worked on non-destructive monitoring systems for process anomalies to improve the process reliability in WAAM. Anomalies are indicated by irregular behaviour compared to the stable system and are, by definition, rare [20]. Spectroscopy can be used to obtain more information about the process, e.g. regarding element distribution or process stability, by analysing the entire spectrum of emitted wavelengths [21–23]. Ma et al. have proven that laser opto-ultrasonic dual detection can be used for simultaneous compositional, structural, and stress analyses of parts manufactured by WAAM [21]. Huang et al. used a spectrometer for monitoring the dynamic behaviour during WAAM of aluminium and found that when the current in the process increased, the intensity in the spectral wavelengths increased accordingly [22]. Zhao et al. observed additional peaks in the light emission spectrum during WAAM of steel without shielding gas compared to WAAM of steel with shielding gas and were the first ones to show that a spectrometer can be used as a monitoring system in WAAM [23]. Zhao et al. investigated, among other spectral emissions, in particular the oxygen spectrum with a wavelength of 777.19 nm to detect rust ($Fe_2O$) [23]. Reisch et al. proposed a context-sensitive, multivariate monitoring system to ensure the required quality of the parts produced by WAAM using different sensors such as current and voltage sensor to detect oxidation anomalies [24,25]. In-situ monitoring systems for oxidation anomalies are of high interest for an autonomous manufacturing system, which should detect the occurrence of oxidation anomalies in order to initiate countermeasures to prevent further oxidation anomalies or to stop the process due to insufficient part quality. Such a monitoring system would increase process stability and would be a further step towards one-piece production. In the present work, a monitoring system based on Light Emission Spectroscopy was investigated to observe the occurrence of such oxidation anomalies.

WAAM of aluminium has great potential to be widely used in industry, but it is still a process that needs further research to understand all phenomena and to ensure high quality parts. In the present work, oxidation effects in WAAM parts (mainly related to the gas flow rate) were analysed. Two main effects were analysed; the surface oxidation on aluminium parts and the oxidation anomalies within aluminium parts, to increase the understanding and the potential control of these effects. A monitoring system based on spectral analysis was introduced, to detect oxidation anomalies during WAAM. Computational Fluid Dynamics (CFD) simulation for different gas flow rates, nozzle-to-work distances, and robot travel speeds were performed, to support and extend the experimental results.

## 2. Material and methods

### 2.1. Materials and experimental set-up

Four walls were manufactured by WAAM with decreasing gas flow rates, from 10 to 4 l/min. The experiments were carried out with a wire of AlSi5(wt%) and a wire diameter of 1.2 mm. AlSi5(wt%) was used because it is one of the most commonly and successfully used alloys for welding applications, making it a promising alloy for WAAM. Substrate plates of AlMg1SiCu(wt%) with the dimensions 120 × 100 × 5 mm were used as this aluminium alloy is one of the most common alloys for such extruded profiles and is found in many applications. The chemical compositions of the two alloys are shown in Table 1.

The equipment used for the experiments is shown in Fig. 1. For the robot-based WAAM, a 6-axis robot (Comau, ITL), a motion control (Siemens, GER), and a welding source with CMT functionality (Fronius, AT) were used. For monitoring of the WAAM process, a welding camera (Cavitar, FIN), a spectrometer (Oceanoptics, UK, Measurement range: 190–1020 nm), a pyrometer (Optris, GER, Measurement range: −50 to 900 °C), and two NiCr-Ni thermocouples (Measurement range: −220 to 1150 °C) with a data logger (Almemo, GER) were used. In addition to the process imaging with the welding camera, high-speed videos in the first and second layer were recorded with 2000 frames per second.

The experiments were conducted by WAAM with a torch perpendicular to the substrate, as shown in Fig. 2. In the experiments, a wall was built by processing ten layers on top of each other with a track

**Table 1**
Chemical composition of the aluminium alloys used, in wt% [26].

| Alloy | Al | Si | Fe | Cu | Mn | Mg | Zn | Cr | Ti |
|---|---|---|---|---|---|---|---|---|---|
| AlSi5 | Bal. | 4.5–6 | 0.8 | 0.3 | 0.05 | 0.05 | 0.1 | – | 0.2 |
| AlMg1SiCu | Bal. | 0.4–0.8 | 0.7 | 0.15–0.4 | 0.15 | 0.8–1.2 | 0.25 | 0.04–0.35 | 0.15 |

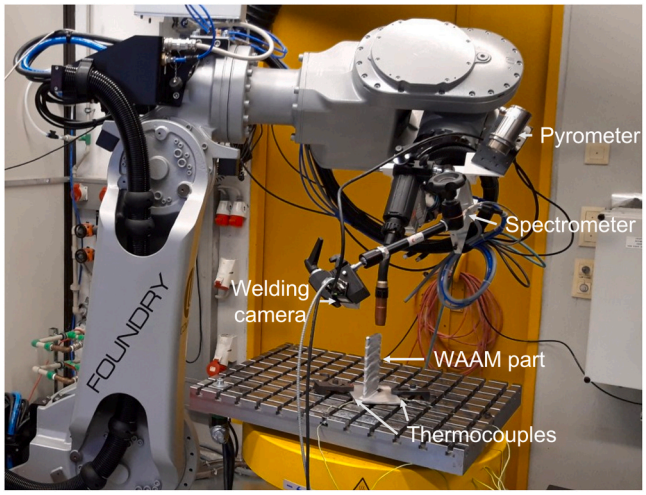


**Fig. 1.** Set-up of the robot based WAAM cell.

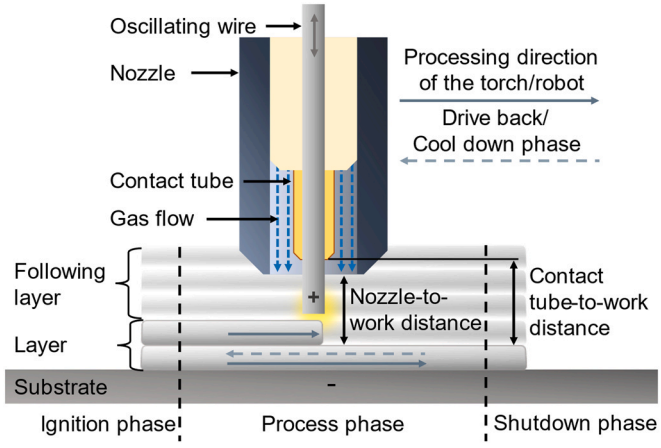


**Fig. 2.** Schematic torch set-up for layer-by-layer part production.

height of 1.5–2.0 mm and a length of 80 mm. The first two layers were produced in the Pulsed Cold Metal Transfer (CMT+P) mode to achieve a better bonding to the substrate due to the higher energy input in this process mode. After the first two layers, the process mode was switched to the CMT mode. In order to create a smooth wall in terms of temperature balance, the wire feed speed was reduced from 5 m/min in the first layer to 4 m/min in the second layer to 3 m/min in the third layer and was kept stable from that layer on. The build strategy involved material being deposited in one direction only. After each track the torch was moved back, resulting in a cooling time of five seconds between the layers. In the CMT and CMT+P processes, each layer in the experiments consists of an ignition phase, a process phase, and a shutdown phase. In the ignition phase, the energy input is higher to initiate the arc-based process. In the process phase the set parameters are used, and in the shutdown phase the robot stops its movement but continues the deposition to fill the end zone using a lower power level. The parameters used for the experiments are listed in Table 2. The main parameter, modified in the physical experiments, was the gas flow rate, which was manually

**Table 2**
Process parameters used for WAAM of AlSi5(wt%).

| Parameter | Value |
|---|---|
| Wire material | AlSi5(wt%) |
| Wire diameter | 1.2 mm |
| Substrate material | AlSi1MgMn(wt%) |
| CMT+P mode | Mode 881 |
| CMT mode | Mode 1658 |
| Ignition phase | 10 mm |
| Process phase | 60 mm |
| Shutdown phase | 10 mm |
| Wire feed speed | 3–5 m/min |
| Robot travel speed | 0.35 m/min |
| Shielding gas | Argon |
| Gas flow rate | 4–10 l/min |
| Nozzle-to-work distance | 14 mm |
| Contact tube-to-work distance | 16 mm |
| Torch angle | Neutral (0°) |

controlled by a flow metre. In the validation experiments for the performed simulations and the monitoring approach of oxidation anomalies, further parameters such as nozzle-to-work distance, process mode, and robot travel speed were changed.

### 2.2. In-situ monitoring sensors

In order to monitor and analyse the melt pool during WAAM, regarding oxidation effects, a Cavitar C200 was employed. The welding camera was used to monitor the melt pool at an angle of 30° to the horizontal from the front with a frame rate of 30 images per second. For very bright processes such as WAAM, a laser is used to illuminate the process at a specific wavelength, while all other process-related radiation outside the wavelength of 640 nm are blocked by a band pass filter to obtain a non-saturated view on the melt pool as shown in Fig. 3a. Oxidation anomalies can also be detected in the process images as shown in Fig. 3b.

An Oceanoptics USB2000+ spectrometer from Ocean Insight, which can detect the intensity of wavelengths from 200 nm to 1000 nm, was used to monitor process-related emissions. The energy released from the redox reaction of aluminium with oxygen should be detectable in the intensity of the spectral wavelengths, and thus correlate with oxidation anomalies. For the experiments, specific wavelength ranges of 20 nm were used to average the values over a defined range to avoid a noisy

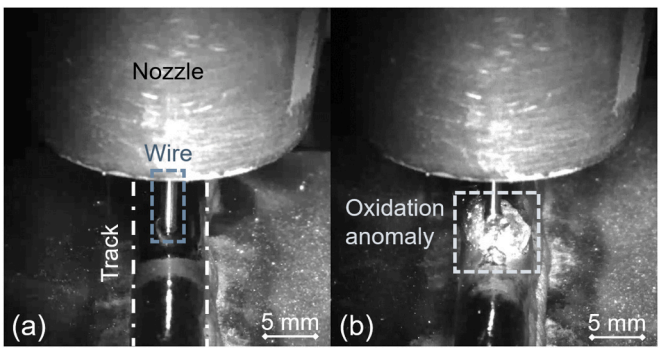


**Fig. 3.** Process images (a) in the regular WAAM process and (b) once an oxidation anomaly occurs.

sensor signal. Before the experiments were conducted, the environmental spectrum was recorded to compare it with the spectrum during a stable WAAM process to identify the significant wavelengths induced by WAAM, as shown in Fig. 4. The comparison of the spectra revealed significant peaks in the ultraviolet (UV) wavelength range of 300–320 nm, in the visual (VIS) wavelength range of 380–400 nm, and in the infrared (IR) wavelength range of 800–820 nm, which are highlighted in Fig. 4. In addition to these significant wavelengths, characteristic oxygen wavelengths such as 460–480 nm (value from the spectrometer), 620–640 nm (value from the spectrometer), and 770–790 nm (value from [23]) were used. In the UV spectrum one further wavelength range of 220–240 nm was monitored to get at least two wavelength ranges from each spectrum (UV, VIS, and IR). The timeseries data of all these wavelength ranges, highlighted in Fig. 4, during the processing were measured, analysed and compared for all the experiments with different gas flow rates, especially regarding oxidation anomalies. The timeseries data were captured with a frequency of 100 Hz.

For collecting temperature data during WAAM, a pyrometer with a measurement range from −50 to 900 °C, and two NiCr-Ni thermocouples with a measurement range from −220 to 1150 °C, were used. The pyrometer was mounted on the robot and moved with the torch. The thermocouples were attached to the substrate, as shown in Fig. 1. The three sensors together provide reliable information about the process temperature.

### 2.3. Material analysis

A Scios DualBeam system (Thermo Fisher Scientific, USA) was used for scanning electron microscope (SEM) images and Energy-dispersive X-ray spectroscopy (EDX) to analyse the material composition of the test sample shown in Fig. 5. EDX line scans were used to analyse the element distribution in the material transition from the surface oxidation film to the inner aluminium alloy in the regions shown in Fig. 5c. Hauser et al. have determined that EDX is suitable for analysing the material transitions of multi-material parts [27]. The EDX line scans were used to analyse the thickness of the surface oxidation in different regions of the wall. For that reason the main elements aluminium, silicon, and oxygen were analysed. The thickness of the surface oxidation was defined by measuring the range in which the detected oxygen and aluminium elements rise in the EDX line scans until the element distribution of aluminium and silicon reaches over 95%.

### 2.4. Computational fluid dynamics model

In order to understand the influence of the gas flow rate on the gas flow behaviour and its consequences in WAAM, CFD simulations were used to visualise and analyse the shielding gas flow on a flat substrate for different operating scenarios. Siemens STAR-CCM+ was used to simulate different cases. The CFD simulation of the gas flow was performed in the process zone with a polyhedral mesh as shown in Fig. 6. The base mesh size in the coarse areas is around 1 mm and in the fine areas around 0.4 mm. Furthermore, along the solid part contours six prism layers were generated to capture the near wall effects. In the CFD simulations of different gas flow rates, the WAAM torch was approximated to an axi-symmetrical domain in which the two-dimensional axi-symmetrical mesh is generated that is assumed to be swept at an angle of 1 radian. In addition to the gas flow rate, the influence of the robot travel speed on the residual oxygen concentration was simulated. For the CFD simulation investigating different robot travel speeds a three-dimensional model was used to investigate the behaviour of the gas flow for different travel speeds. For all simulation cases, the gas flow was considered to be a laminar flow and was computed by the Reynolds-Averaged Navier-Stokes model. The gas flow was modelled as a multi-component ideal gas with two miscible phases of argon and air. Since the flow conditions in WAAM do not change over time, a steady state simulation was performed. Furthermore, a segregated flow solver and iso-thermal condition were applied in the simulation.

The CFD simulation was validated by experimentally measuring the concentrations of residual oxygen in the gas flow with a residual oxygen metre from Orbitalum. In the residual oxygen measurements, a pump beneath the substrate sucks the gas mixture from the process zone through a small hole in the substrate, marked in Fig. 6, and provides a real-time measurement of the oxygen concentration in parts per million (ppm). Measurements were carried out in the centre of the process zone as well as in the outer regions, especially in the cross over from the argon atmosphere to the oxygen-rich environment. Oxygen concentrations

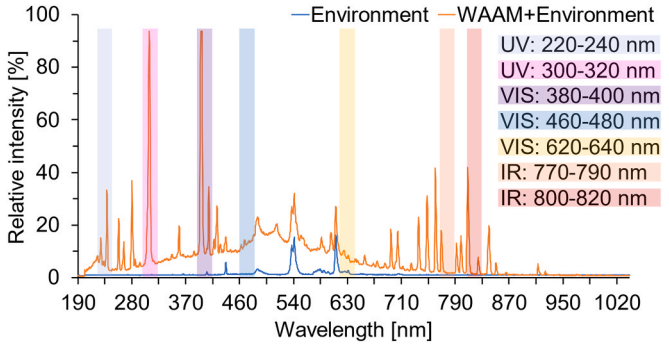


**Fig. 4.** Relative intensity of the emitted spectrum without WAAM (blue course) and during WAAM at a gas flow rate of 10 l/min (orange course) with the highlighted ultraviolet (UV), visual (VIS), and infrared (IR) wavelength ranges which were investigated for monitoring of oxidation anomalies. (For interpretation of the references to colour in this figure legend, the reader is referred to the web version of this article.)

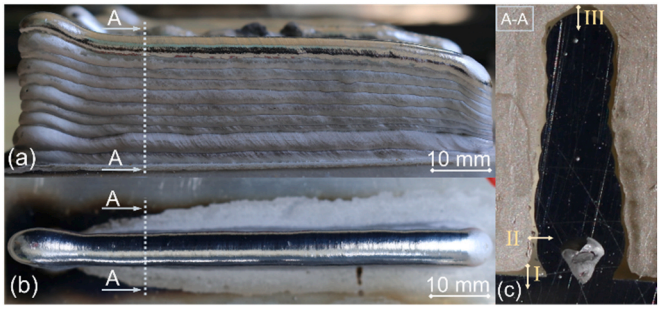


**Fig. 5.** (a) Side view and (b) top view of the aluminium wall manufactured by WAAM at a gas flow rate of 10 l/min with its (c) cross-section A-A with different regions of interest on the substrate (I), on the sidewall (II), and on the top of the wall (III) analysed by EDX line scans.

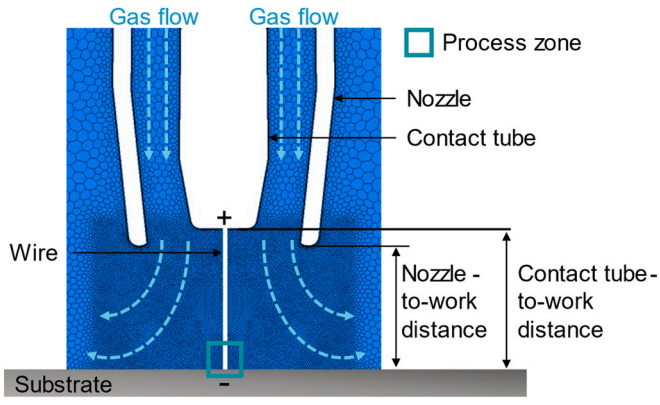


**Fig. 6.** Mesh of the WAAM torch in the CFD simulation (Section through the nozzle centre).

from 0 ppm to 999 ppm could be measured with the residual oxygen metre and the measurements showed a maximum deviation of 40 ppm from the simulation.

## 3. Results

### 3.1. Surface oxidation on aluminium parts manufactured by WAAM

On the aluminium walls manufactured by WAAM, a white film on the surface was observed, as shown in the test sample of Fig. 5. It was found that this white surface was bonded to the wall and could not simply be washed off, indicating that the white surface was surface oxidation. The high-speed images in Fig. 7 revealed, that the arc formed the white surface oxidation during the deposition process in the ignition phase of every CMT cycle when the short-circuit and arc extinction took place. In the first layer, the arc influenced the whole area around the wire and led to a white surface oxidation on the substrate along the whole wall, which was about 20 mm wide and 100 mm long. In the subsequent layers, the procedure was similar as shown in the second layer (Fig. 7b). The arc influenced the previously deposited layer and formed a white oxidation layer on the sides of the layers as well as on the top of the layer (in processing direction). However, the white surface oxidation on the top of the layer remelted by the subsequent CMT cycles and disappeared again. Therefore, on the sidewall the white oxidation layer remained and on the top of the wall it did not but instead a transparent surface oxidation appeared after deposition.

SEM images and EDX line scans were performed on the edges of the substrate (I), the sidewall (II), and on the top of the wall (III), shown in the cross-section of Fig. 5, to analyse the elemental composition and thickness of the surface oxidation in these regions. The areas in which the EDX line scans were carried out are shown in the SEM images of Fig. 8. The EDX line scans and the determined thickness of the surface oxidation is visualised by yellow dotted lines in Fig. 9. The surface oxidation on the substrate (5 μm) was significantly thicker than on the sidewall (3 μm) or on the top of the wall (2.5 μm). In addition, the proportion of oxygen significantly differed. On the substrate, the oxygen content was up to one half as the aluminium content. On the sidewall and on the top of the wall, the content was less than one eighth of the aluminium content. In the oxide layer on the substrate, aluminium and oxygen peaks were observed.

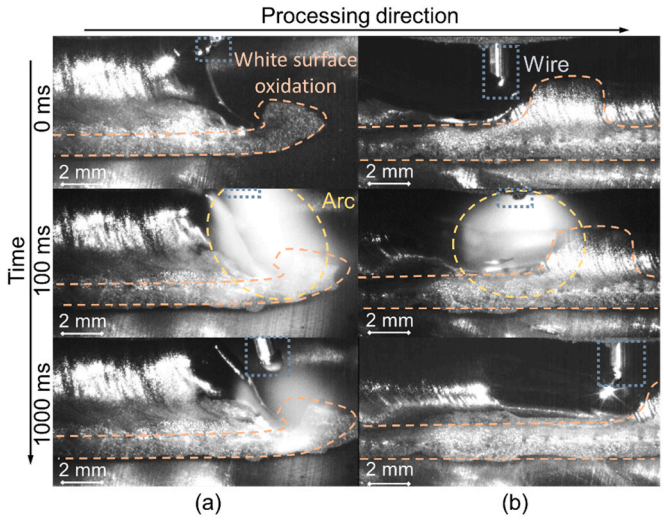


**Fig. 7.** High-speed images of the processing zone in the (a) first and (b) second layer which show the white surface oxidation (marked orange), the arc (marked yellow), and the wire (marked blue). (For interpretation of the references to colour in this figure legend, the reader is referred to the web version of this article.)

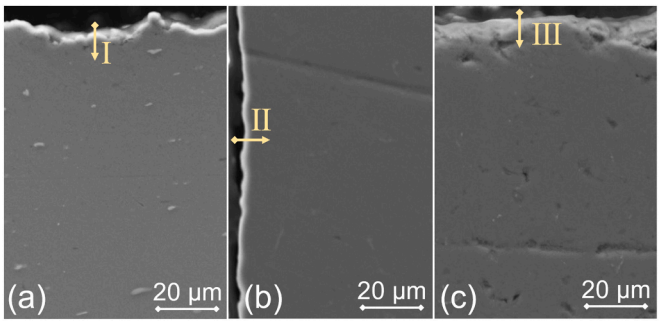


**Fig. 8.** SEM images on (a) the substrate (I), on (b) the sidewall of the first layer (II), and on (c) the top of the wall in the tenth layer (III).

### 3.2. Oxidation anomalies in WAAM of aluminium alloys

The walls manufactured at gas flow rates of 10 l/min, 8 l/min, 6 l/min, and 4 l/min with their corresponding process images of the process camera are shown in Fig. 10. In the wall manufactured at a gas flow rate of 4 l/min, significant disruptions in the wall geometry and in the process images were detected. In the first two layers of the wall manufactured at a gas flowrate of 4 l/min, oxidation anomalies appeared along the whole track as shown in the process image of Fig. 10d. In the subsequent eight layers, the oxidation anomalies occurred randomly in some layers but mainly in the centre of the track, without recognisable trends, as shown in the side view of the wall (Fig. 10d). The oxidation anomalies showed a whitish surface and were the same as those which occurred in WAAM of aluminium without any inert gas. Furthermore, in all experiments black soot appeared in the first layer (visible in the top views of the walls). The black soot consist mainly of alumnium, magnesium, and oxygen [28]. The black soot only formed in the first layer, as the substrate alloy contained magnesium and the wire alloy did not. The amount of black soot increased as the gas flow rate decreased due to less shielding from the environment. In all walls except the wall manufactured at a gas flow rate of 4 l/min, the black soot appeared only in the beginning of the first layer (left side of the wall). Furthermore, in the process images of all experiments a trend in the white surface oxidation was visible because the white surface oxidation became smaller and less intense for a decreasing gas flow rate before it completely disappeared at a gas flow rate of 4 l/min.

In order to investigate the influence of the gas flow rate on oxidation effects during WAAM, the argon gas flow was simulated in its interaction with the ambient air. Fig. 11 shows the scalar plots of the oxygen concentration at gas flow rates from 10 l/min to 4 l/min. The simulation results in Fig. 11 revealed that at a gas flow rate of 4 l/min, the residual oxygen concentration in the process zone increases at lower gas flow rates. The oxygen concentration in the process zone at a gas flow rate of 4 l/min is three times higher as at a gas flow rate of 6 l/min and five times higher as at a gas flow rate of 8 l/min or 10 l/min.

Besides these four main experiments, simulations and validation experiments for different gas flow rates and nozzle-to-work distances were performed. Fig. 12 shows the influence of different nozzle-to-work distances and gas flow rates on the residual oxygen concentration in the centre of the process zone (Fig. 6). It was observed that the argon gas flow rate can be reduced for closer nozzle-to-work distances to achieve a similar level of residual oxygen concentration. According to these experiments, the process was stable at a nozzle-to-work distance of 14 mm and a gas flow rate of 6 l/min. At a gas flow rate of 4 l/min oxidation anomalies occurred at the same nozzle-to-work distance. However according to the simulations (Fig. 12) no oxidation anomalies occur at a nozzle-to-work distance of 10 mm and a gas flow rate of 3 l/min, but oxidation anomalies occur at a nozzle-to-work distance of 14 mm and a gas flow rate of 4 l/min. In validation experiments this behaviour was confirmed. According to the simulations and the validation experiments,

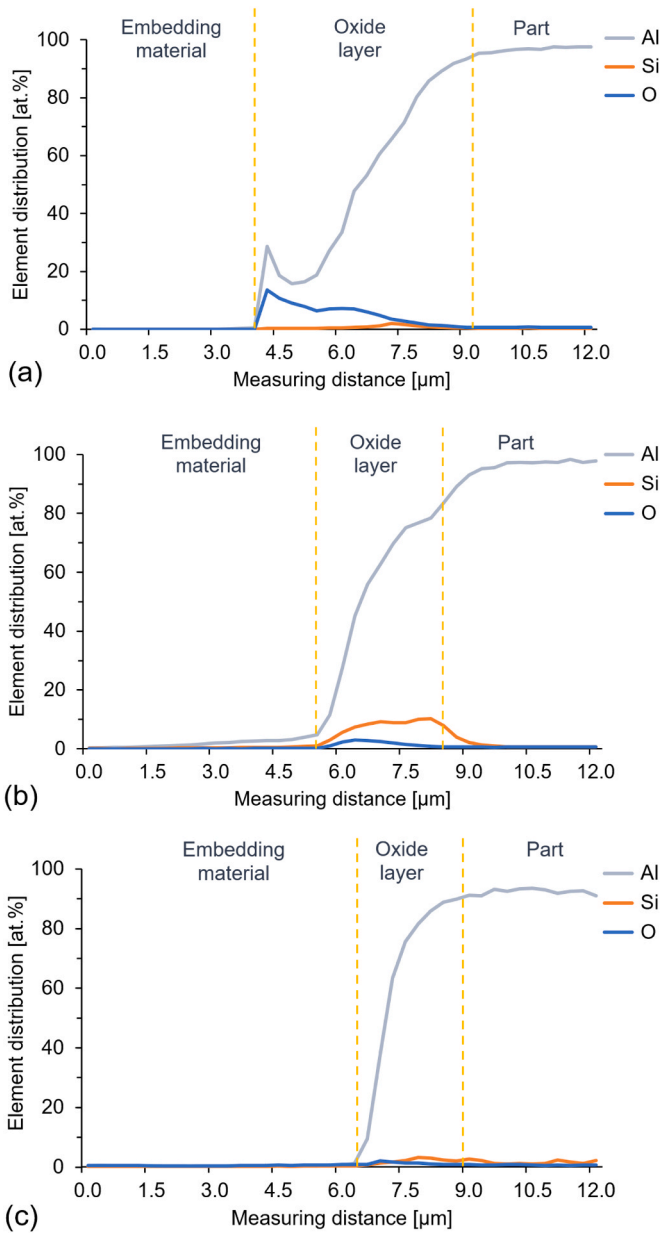


**Fig. 9.** EDX line scans of the element distribution of aluminium (Al), silicon (Si), and oxygen (O) on the edges of a cross-section of the aluminium wall (Fig. 5) on (a) the substrate (I), on (b) the sidewall of the first layer (II), and on (c) the top of the wall in the tenth layer(III). (For interpretation of the references to colour in this figure legend, the reader is referred to the web version of this article.)

oxidation anomalies occur at an oxygen concentration above 100 ppm. Therefore, the maximum residual oxygen concentration should be below 100 ppm, as shown in Fig. 12, to avoid oxidation anomalies.

In addition to the gas flow rate, the influence of different robot travel speeds on the residual oxygen concentration were simulated for a gas flow rate of 10 l/min. The simulation results in Fig. 13 revealed a shift of the area covered by the argon gas flow against the processing direction as the robot travel speed increases. The simulation results revealed that the residual oxygen concentration in the processing zone is twice as high at a robot travel speed of 600 mm/min and four times as high at a robot travel speed of 1500 mm/min as at a robot travel speed of 300 mm/min. However, in the validation experiments, no oxidation anomalies occurred.

### 3.3. Monitoring of oxidation anomalies by light emission spectroscopy

A wall, shown in Fig. 14, was manufactured at changing parameters such as process mode, gas flow rate, and robot travel speed to investigate these parameters regarding the occurrence of oxidation anomalies. Furthermore, the monitoring of these oxidation anomalies by light emission spectroscopy was investigated. In the experiment, the general process parameters, listed in Table 2, were used and kept constant apart from the changing parameters shown in Fig. 15. In the time series data of the observed wavelength ranges (Fig. 4) significant variations in the data, shown in Fig. 15, were observed when oxidation anomalies in the process occurred.

In general, the intensities in the ignition phase of the arc in a new layer are always very high even if no oxidation anomalies occur. Particularly in the CMT+P mode, the ignition phase caused significant peaks in all wavelength ranges. The overall intensity of the process emissions in CMT+P mode was twice as high as in the CMT mode. In the second layer an oxidation anomaly was created by temporarily reducing the shielding gas flow rate to zero. In Fig. 15 these oxidation anomalies are highlighted red. In the UV wavelength range 300 nm to 320 nm, and in the VIS wavelength range 380 nm to 400 nm, significant peaks were detected when oxidation anomalies occurred. In the UV wavelength range 220–240 nm and VIS wavelength ranges 460 nm to 480 nm and 620 nm to 640 nm peaks were also detected, but much less significant. In the IR wavelength range 770 nm to 790 nm, no peaks were detected. In the wavelength range 800 nm to 820 nm, the emissions even decreased when the oxidation anomalies occurred. In the third layer (switched to CMT mode), no subsequent oxidation anomalies were found but still small peaks were detected at the location where oxidation anomalies occurred in the second layer. In the fourth layer no further influence of the oxidation anomalies from the second layer was detected in the data.

In the fifth layer, oxidation anomalies were created in the CMT mode as for the CMT+P mode in the second layer. All wavelength ranges showed the same behaviour as in the second layer when oxidation anomalies occurred. In the following sixth layer the behaviour was the same as for the third layer and in the seventh layer the behaviour was again the same as in the second and fifth layer even for a, in general, lower gas flow rate of 6 l/min. From the eighth layer on, the robot travel speed was increased. Despite the increase in robot travel speed, no oxidation anomalies occurred, but still small peaks were detected at the location where oxidation anomalies occurred in the previous deposited layer. In the ninth layer no oxidation anomalies were found, and no peaks were detected. From the tenth layer on, the robot travel speed was increased again to 1500 mm/min but still no oxidation anomalies were found. Although the robot travel speed was four times as high as in the first layers no oxidation anomalies occurred in the tenth and eleventh layer and no peaks were detected. In the last layer, the process mode was switched to CMT+P with a robot travel speed of 1500 mm/min and a gas flow rate of 6 l/min but still no oxidation anomalies occurred. Although no peaks but only a generally higher intensity due to the CMT+P mode was found in the data.

## 4. Discussion

### 4.1. White surface oxidation of parts manufactured by WAAM

It was observed that on the substrate and on the sidewalls a white surface oxidation formed. Only on the top of the wall no white but a transparent surface oxidation formed. It is indicated by the experiments with different gas flow rates that the observed white surface oxidation on the part formed in the area around the melt pool where the plasma of the arc acts. The white surface oxidation does not form directly after the deposition, but when the next layer is deposited on top of or next to this layer. Therefore, it turns white after the next layer has been deposited. Since this area is covered by inert gas and thus a very low amount of

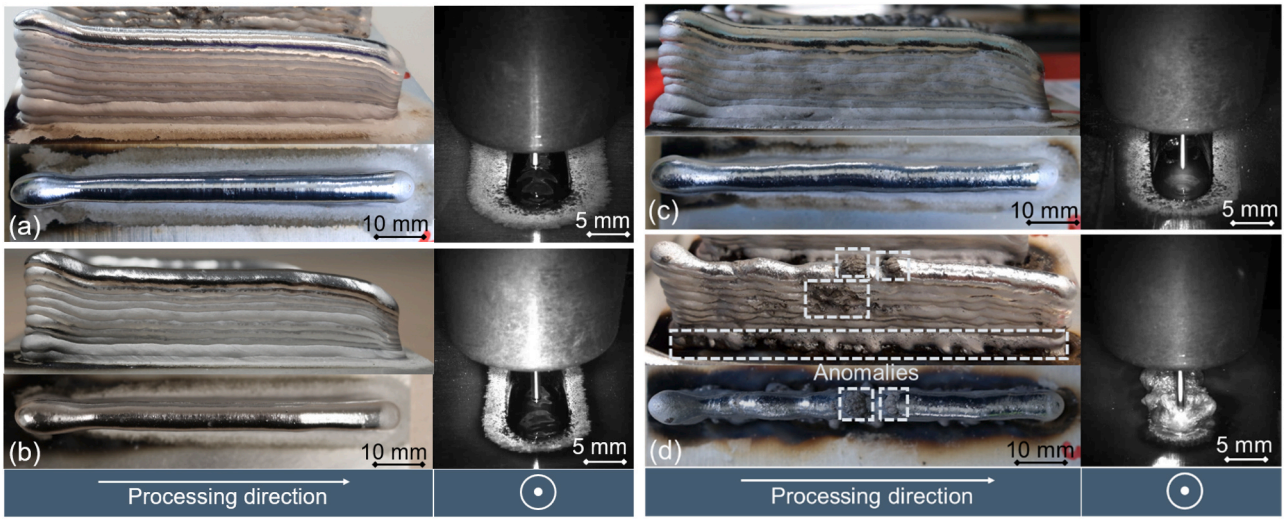


**Fig. 10.** Resulting walls (side and top view) and process images in the first layer for WAAM with gas flow rates of (a) 10 l/min, (b) 8 l/min, (c) 6 l/min, and (d) 4 l/min.

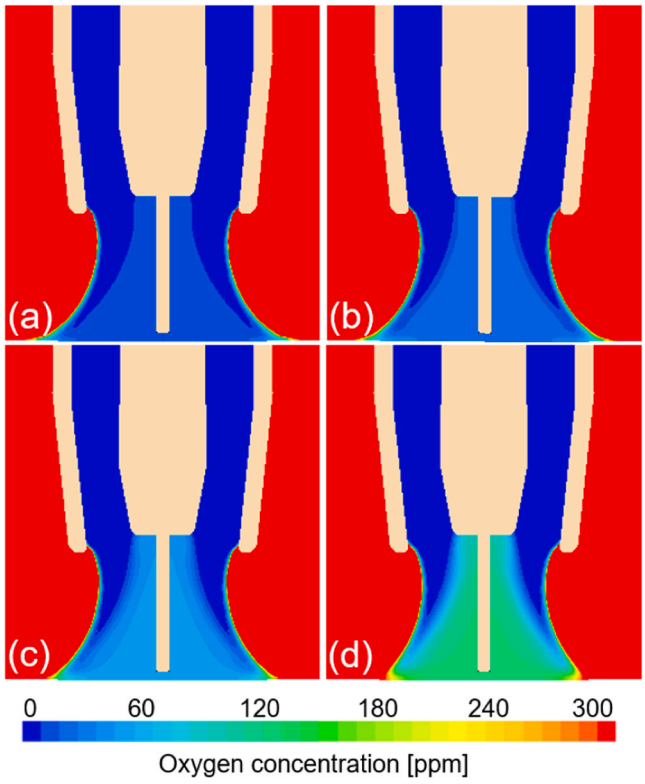


**Fig. 11.** Argon gas flow in a cross-sectional view in interaction with the oxygen-rich atmosphere for (a) 10 l/min, (b) 8 l/min, (c) 6 l/min, and (d) 4 l/min.

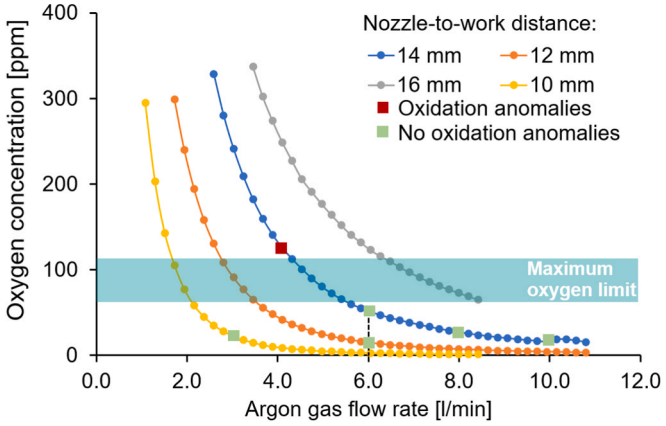


**Fig. 12.** Progression of the relative oxygen concentration in the centre of the process zone for different gas flow rates and nozzle-to-work distances from simulation results (lines) and experimental validation experiments (square points) with the maximum oxygen limit for oxidation anomalies (green marked area). (For interpretation of the references to colour in this figure legend, the reader is referred to the web version of this article.)

oxygen/ambient air is available to react with the aluminium, it was assumed that the thickness and element composition of the oxide layer does not significantly change. The thickness and element composition of the surface oxidation was analysed by EDX scans on the substrate, on the sidewall and the top of the wall. The results revealed a decrease in thickness and oxygen content of the surface oxide layer between the substrate and the layers, manufactured by WAAM. The reason for the reduced oxide layer thickness at higher wall position can be related to the nature of the oxide skin creation and its dependence on time and temperature, while longer time and higher temperatures increase diffusion effects. The diffusion effect continues over a relatively long time period due to the permanent heat input of the arc and the high conductivity of the aluminium, which keeps the entire part heated. In addition, the substrate already had a surface oxidation layer before processing, which has grown over time and explains the thicker surface oxidation. Aluminium and oxygen peaks were also observed in the EDX line scans of the substrate, which most likely occurred during the deposition of the first layer when the arc acted on the existing oxidation layer of the substrate. Since neither on the side wall nor on the top of the wall such a thick oxide layer could form, such peaks were not observed in those areas. However, the EDX line scans showed that the content and thickness of the surface oxidation between the sidewall and the top of the wall did not significantly differ.

Therefore, it can be assumed that the white colour of the surface oxidation is not caused by the thicker oxide layer or a different element composition. Furthermore, the interpass temperature during processing, recorded with the pyrometer and the thermocouples, showed for the whole part, except the melt pool, wherein the process is above the melting temperature of aluminium (>660 °C), a maximum temperature of 250 °C. During WAAM the deposited material solidifies and adapts to

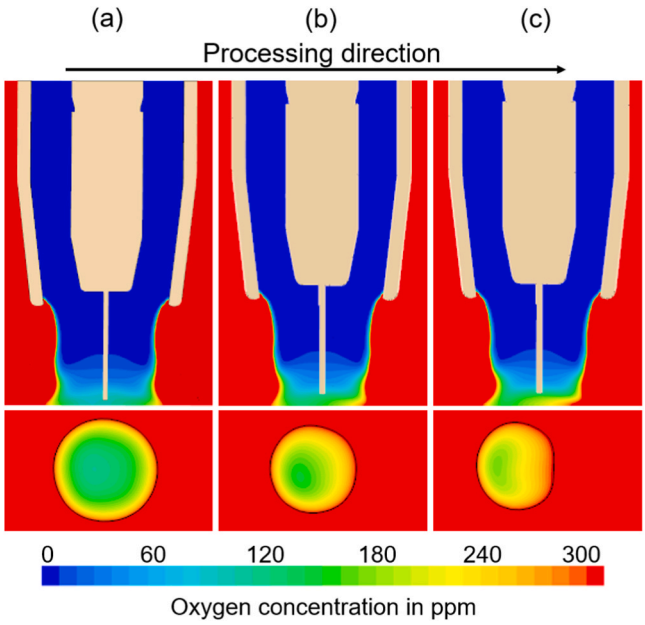


**Fig. 13.** Argon gas flow through the nozzle at 10 l/min in interaction with the oxygen-rich atmosphere for different robot travel speeds of (a) 350 mm/min, (b) 600 mm/min, and (c) 1500 mm/min in side and top views.

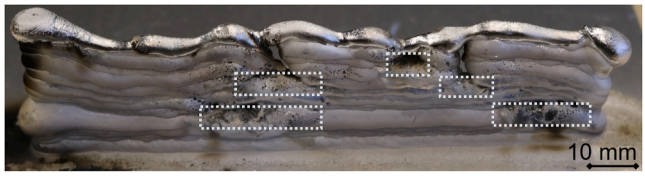


**Fig. 14.** Twelve-layer wall with local forced oxidation anomalies in the second, fifth, and seventh layer (white dashed lines).

this interpass temperature. This heat balance occurs due to the high conductivity of aluminium (237 W/mK), within the inert gas atmosphere.

Therefore, no duplex oxide layer but a transparent amorphous oxide layer forms right after deposition, just at the moment when the heated layer comes into contact with the ambient air, as shown in Fig. 16. At high temperatures above 300 °C, a duplex oxide layer containing both crystalline and amorphous oxides is formed instead of a pure amorphous oxide layer which is formed at ambient temperature [15]. The high-speed videos revealed that the observed white surface oxidation on the part formed in the area around the melt pool where the plasma of the arc acted. This indicates that the high temperatures of the arc, reaching up to 10,000 K in the shielding gas [6], transfers enough energy into the existing amorphous oxide layer of the previously deposited layer, that a duplex oxide layer forms.

In all layers, an amorphous surface oxidation formed on the deposited layer and a white surface oxidation formed on the previous deposited layer, as shown in Fig. 16. The crystalline oxides in the duplex oxide layer caused the white colour which can be recognised in the high-speed images and on the walls manufactured. For that reason, the surface oxidation in the last layer was not white but transparent because only an amorphous oxide layer (which is mainly transparent) formed. Consequently, it can be stated that the effect of the high temperatures of the arc on the material surface turns the existing, amorphous, and transparent surface oxidation of the previously deposited aluminium layer into the white, duplex oxide layer. On the substrate, the white surface oxidation was along the whole wall about 20 mm wide, which indicates that the arc acted with a radius of about 10 mm. In the same way as the arc affected the sides, it also affected the previous deposited layers below, as shown in Fig. 16. Furthermore, the process images and the manufactured walls showed, that the area affected by the arc increased with a higher gas flow rate, as the area with white surface oxidation on the substrate also increased.

### 4.2. Parameters influencing oxidation anomalies in WAAM parts

The reason for the oxidation anomalies in the wall manufactured at a gas flow rate of 4 l/min, was the inadequate shielding, which was also shown in the simulation results (Fig. 11). In addition to the oxidation anomalies, black soot occurred over the entire first layer for the wall manufactured at 4 l/min, which is also a sign of inadequate shielding (at least for aluminium alloys without a high content of magnesium). The experimental results were validated by CFD simulations, which matched with the appearance of the oxidation anomalies and the higher amount of black soot in the experiments. The simulations results revelead that the oxygen concentration in the process zone at a gas flow rate of 4 l/min was three times higher than at a gas flow rate of 6 l/min. Further simulations on the influence of different nozzle-to-work distances and changing gas flow rates revealed an increase of residual oxygen concentration with an increase in the nozzle-to-work distance or a reduction of the gas flow rate. This correlation can be explained since with a lower gas flow rate and a bigger nozzle-to-work distance, the interaction with the oxygen-rich atmosphere also increases, as shown in the simulation results (Figs. 11 and 12). WAAM is based on the deposition of individual melt droplets, that melt from the end of the wire, and form together a layer. The high amount of oxygen reacts with these melt droplets and forms an aluminium surface oxide ($Al_2O_3$) around. Due to this aluminium surface oxide the melt droplet does not join with the so far deposited layer, causing the oxidation anomaly. As with the white surface oxidation, the oxidation anomalies show a whitish surface, which is caused by the oxidation in the moment of melting the wire. The oxidation therefore takes place at a very high temperature of about 660 °C, which is the reason that a duplex oxide layer forms around the melt drop, causing the whitish oxidation anomaly.

In addition to the parameters of gas flow rate and nozzle-to-work distance, the process mode (CMT or CMT+P) and the robot travel speed were also investigated. The oxidation anomalies in the wall manufactured at 4 l/min occur randomly, except for the first two layers. In these two layers the energy input was much higher due to a higher wire feed rate and the CMT+P mode. All experiments showed more oxidation anomalies for the CMT+P mode as for the CMT mode and for a higher wire feed rate as for a lower wire feed rate. Thus, the oxidation anomalies are likely caused by higher disturbances of the shielding gas with the oxygen-rich atmosphere although the gas flow rate and the nozzle-to-work distance do not change. These disturbances are likely related to the higher heat input and the pulses in the CMT+P mode, which lead to a more dynamic process and cause turbulence in the shielding gas and thus a mixing with the ambient air. Consequently, oxidation anomalies are more likely to appear in the CMT+P mode and thus a higher shielding gas flow rate is necessary to avoid oxidation anomalies. The increase of oxidation anomalies with a higher wire feed rate was caused by the higher amount of material deposited, which implies that a larger area must be shielded with the same gas flow rate.

Furthermore, the influence of the robot travel speed on the shielding gas was simulated and it was shown that with a higher robot travel speed, the residual oxygen concentration in the process zone increases linearly. However, validation experiments showed no increase in oxidation anomalies for a higher robot travel speed. This fact is probably caused due to the less deposited material with a higher robot travel speed, which implies that a smaller area must be shielded with the same gas flow rate. Additionally, the shielded area shifts to positions behind the processing zone in which the previous deposited material cools down and solidifies. Therefore, the crucial area for oxidation anomalies was still shielded.

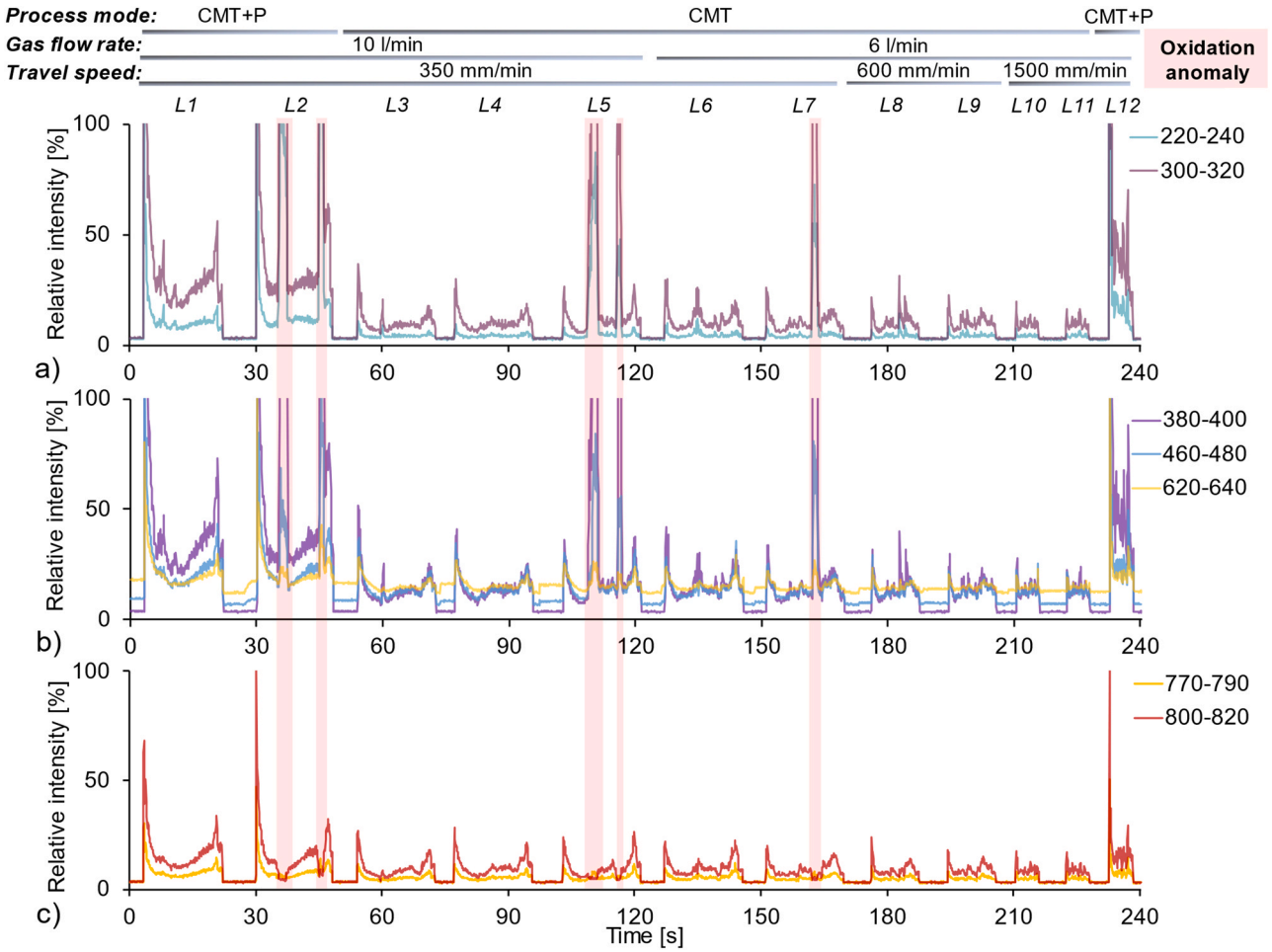


**Fig. 15.** Relative intensity for the (a) UV wavelength ranges, (b) VIS wavelength ranges, and (c) IR wavelength ranges during WAAM of the manufactured twelve-layer wall, shown in Fig. 14, with locally forced oxidation anomalies highlighted in red. (For interpretation of the references to colour in this figure legend, the reader is referred to the web version of this article.)

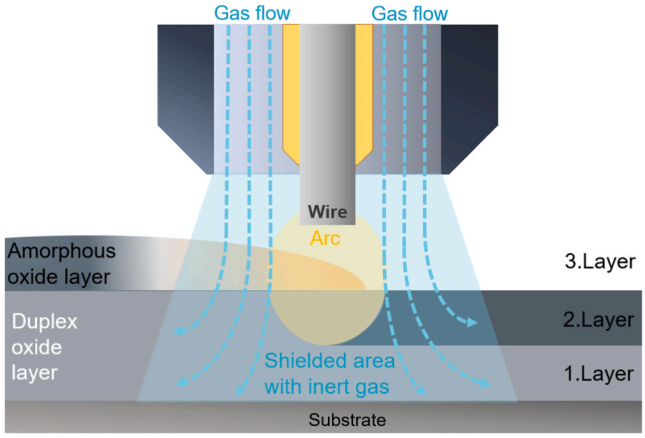


**Fig. 16.** Schematic in the formation of the white surface oxidation in WAAM.

In summary, a minimum gas flow is necessary to protect the processing zone from oxidation anomalies. Oxidation anomalies are influenced by different process parameters such as the gas flow rate, the nozzle-to-work distance, the process mode, the wire feed rate and the robot travel speed with an impact summarised in Table 3. The impact of the specific parameters was classified into three categories (high, medium, and low) based on the visual inspection of the appearance and size of oxidation anomalies. The maximum residual oxygen concentration in the centre of the process zone should be kept below 100 ppm.

**Table 3**
Impact of different process parameters on shielding from oxidation anomalies.

| Parameter | Impact on oxidation anomalies |
|---|---|
| Gas flow rate | High |
| Nozzle-to-work distance | High |
| Process mode (Heat input) | Medium |
| Wire feed rate | Medium |
| Robot travel speed | Low |

### 4.3. Light emission spectroscopy of oxidation anomalies

In the UV wavelength range from 300–320 nm and in the VIS wavelength range from 380–400 nm, low intensities during regular processing and significant peaks when oxidation anomalies occurred were observed. In the UV wavelength range from 220 nm to 240 nm the intensities of the peaks were less significant as for the UV wavelength range from 300 nm to 320 nm. However, the intensities in the UV wavelength range, from 220 nm to 240 nm, were also lower in the stable WAAM process and thus the relative significance is the same as for the UV wavelength range from 300 nm to 320 nm. In the remaining VIS wavelength ranges, from 460–480 nm and from 620–640 nm, the oxidation anomalies were also detected but the total and relative peaks were not as significant. In the IR wavelength range from 770 nm to

790 nm no peaks were detected. In the IR wavelength range from 800 nm to 820 nm the intensities were even lower when oxidation anomalies occurred. Therefore, the most significant anomaly-related peaks were detected in the wavelength ranges from 220 nm to 240 nm, from 300 nm to 320 nm, and from 380 nm to 400 nm. These peaks were caused by the released energy of the exothermic reaction when the oxidation takes place. This released energy is detected in the light emission spectroscopy.

The reduction in IR emission could be explained by the change in the emission coefficient or the lower reflectance due to the change in surface colour (whitish surface oxidation instead of transparent surface oxidation). However, the fact that only the IR emissions in the wavelength range from 800 nm to 820 nm decreased makes another effect seem more likely. Since for an exothermic reaction, activation energy is needed, this activation energy is extracted from the process and reduced the IR emissions. Thus, the consistent intensities in the IR wavelength range from 770–790 nm and even lower intensities in the IR wavelength range from 800–820 nm were observed.

## 5. Conclusions

In the present work, surface oxidation and oxidation anomalies in Wire Arc Additive Manufacturing of AW4043/AlSi5(wt%) were investigated and the experimental observations were supported by CFD simulations. Furthermore, light emission spectroscopy was used to capture process emission data for a monitoring approach of oxidation anomalies. The following conclusions can be drawn:

- The experiments with different gas flow rates, the corresponding process images, the high-speed videos, and the EDX line scans, showed that the observed white oxidation layer formed in the area around the melt pool where the plasma of the arc acted. Since this area is covered by inert gas and thus a very low amount of oxygen/ambient air is available to react with the aluminium, it can be stated that the high temperatures of the arc turn the existing amorphous surface oxidation, of the previously deposited aluminium layer, into a white duplex oxide layer.
- The decreasing thickness of the surface oxidation from the substrate to the layers manufactured by WAAM can be mainly explained by the existing surface oxidation of the substrate before processing. In addition, the repeated heat input of the arc and the high conductivity of the aluminium, keep the entire part heated and increase diffusion effects during processing.
- If the shielding during WAAM is too low a threshold of oxygen contamination (in the current case: 100 ppm) is exceeded in the processing zone and oxidation anomalies can occur in the part and trigger uneven material accumulations which can be detected by process imaging. These oxidation anomalies also show a whitish surface, indicating a duplex oxide layer. Different from the white surface oxidation, this duplex oxide layer forms immediately when the material is deposited.
- The experiments and simulations showed that shielding decreases with a lower gas flow rate, a process mode with higher heat input (CMT+P), a bigger nozzle-to-work distance, and a higher wire feed rate, while the robot travel speed does not have a measurable impact.
- Light emission spectroscopy can be used to detect changes in the intensity of the emitted spectral wavelengths which were found to correlate with the occurrence of oxidation anomalies due to the exothermic reaction, which takes place when the material oxidises.
- The most significant peaks in the time series data of the spectrometric measurements when oxidation anomalies occurred, were detected in the ultraviolet wavelength ranges, from 220 nm to 240 nm and from 300 nm to 320 nm, and in the visual wavelength range from 380 nm to 400 nm.

## CRediT authorship contribution statement

**Tobias Hauser**: Conceptualization, Methodology, Software, Validation, Investigation, Writing - original draft, Writing - review & editing, Visualization. **Raven Thomas Reisch**: Methodology, Writing - review & editing. **Philipp Peter Breese**: Formal analysis, Investigation, Writing - review & editing. **Yogesh Nalam**: Formal analysis. **Kaivalya S. Joshi**: Investigation. **Katharina Bela**: Investigation, Writing - review & editing. **Tobias Kamps**: Project administration, Funding acquisition, Supervision. **Jörg Volpp**: Project administration, Funding acquisition, Writing - review & editing, Supervision. **Alexander F.H. Kaplan**: Writing - review & editing, Supervision.

## Declaration of Competing Interest

The authors declare that they have no known competing financial interests or personal relationships that could have appeared to influence the work reported in this paper.

## Acknowledgement

The authors gratefully acknowledge funding from EIT RawMaterials (Initiated and funded by the European Institute of Innovation and Technology) for the project SAMOA - Sustainable Aluminium additive Manufacturing for high performance Applications, no. 18079. Furthermore, the authors acknowledge the technical and formal advice by Dr. John Powell (Visiting Professor at Luleå University in Sweden and Nottingham University in UK).

## References

[1] R. Kaibyshev, F. Musin, D.R. Lesuer, T.G. Nieh, Superplastic behavior of an Al–Mg alloy at elevated temperatures, Mater. Sci. Eng. A 342 (2003) 169–177, https://doi.org/10.1016/S0921-5093(02)00276-9.

[2] H. Geng, J. Li, J. Xiong, X. Lin, F. Zhang, Geometric limitation and tensile properties of wire and arc additive manufacturing 5A06 aluminum alloy parts, J. Mater. Eng. Perform. 26 (2017) 621–629, https://doi.org/10.1007/s11665-016-2480-y.

[3] U. Dilthey, Schweißtechnische Fertigungsverfahren 2: Verhalten der Werkstoffe beim Schweißen, Dritte bearbeitete Auflage, Springer-Verlag Berlin Heidelberg, Berlin, Heidelberg, 2005.

[4] Le Zhou, H. Hyer, S. Park, H. Pan, Y. Bai, K.P. Rice, Y. Sohn, Microstructure and mechanical properties of Zr-modified aluminum alloy 5083 manufactured by laser powder bed fusion, Addit. Manuf. 28 (2019) 485–496, https://doi.org/10.1016/j.addma.2019.05.027.

[5] T. DebRoy, H.L. Wei, J.S. Zuback, T. Mukherjee, J.W. Elmer, J.O. Milewski, A. M. Beese, A. Wilson-Heid, A. De, W. Zhang, Additive manufacturing of metallic components – process, structure and properties, Prog. Mater. Sci. 92 (2018) 112–224, https://doi.org/10.1016/j.pmatsci.2017.10.001.

[6] S. Zielińska, K. Musioł, K. Dzierżęga, S. Pellerin, F. Valensi, C. de Izarra, F. Briand, Investigations of GMAW plasma by optical emission spectroscopy, Plasma Sources Sci. Technol. 16 (2007) 832–838, https://doi.org/10.1088/0963-0252/16/4/019.

[7] T. Hauser, A.D. Silva, R.T. Reisch, J. Volpp, T. Kamps, A.F.H. Kaplan, Fluctuation effects in wire arc additive manufacturing of aluminium analysed by high-speed imaging, J. Manuf. Process. 56 (2020) 1088–1098, https://doi.org/10.1016/j.jmapro.2020.05.030.

[8] P. Kazanas, P. Deherkar, P. Almeida, H. Lockett, S. Williams, Fabrication of geometrical features using wire and arc additive manufacture, Proc. Inst. Mech. Eng. Part B J. Eng. Manuf. 226 (2012) 1042–1051, https://doi.org/10.1177/0954405412437126.

[9] A.G. Ortega, L. Corona Galvan, M. Salem, K. Moussaoui, S. Segonds, S. Rouquette, F. Deschaux-Beaume, Characterisation of 4043 aluminium alloy deposits obtained by wire and arc additive manufacturing using a Cold Metal Transfer process, Sci. Technol. Weld. Join. 24 (2019) 538–547, https://doi.org/10.1080/13621718.2018.1564986.

[10] T.A. Rodrigues, V. Duarte, R.M. Miranda, T.G. Santos, J.P. Oliveira, Current status and perspectives on wire and arc additive manufacturing (WAAM), Materials 12 (2019) 1121, https://doi.org/10.3390/ma12071121.

[11] C. Zhou, H. Wang, T.A. Perry, J.G. Schroth, On the analysis of metal droplets during cold metal transfer, Procedia Manuf. 10 (2017) 694–707, https://doi.org/10.1016/j.promfg.2017.07.024.

[12] S. Selvi, A. Vishvaksenan, E. Rajasekar, Cold metal transfer (CMT) technology - an overview, Def. Technol. 14 (2018) 28–44, https://doi.org/10.1016/j.dt.2017.08.002.
[13] H. Shi, C. Tang, A. Jianu, R. Fetzer, A. Weisenburger, M. Steinbrueck, M. Grosse, R. Stieglitz, G. Müller, Oxidation behavior and microstructure evolution of alumina-forming austenitic & high entropy alloys in steam environment at 1200 °C, Corros. Sci. 170 (2020), 108654, https://doi.org/10.1016/j.corsci.2020.108654.
[14] X. Shi-Gang, S. Li-Xin, Z. Rong-Gen, H. Xing-Fang, Properties of aluminium oxide coating on aluminium alloy produced by micro-arc oxidation, Surf. Coat. Technol. 199 (2005) 184–188, https://doi.org/10.1016/j.surfcoat.2004.11.044.
[15] Aluminum Alloys—Contemporary Research and Applications, Elsevier, 1989.
[16] Aluminium-Zentrale, Aluminium-Taschenbuch, Aluminium-Verlag, Duesseldorf, 1988.
[17] G. Campana, A. Ascari, A. Fortunato, G. Tani, Hybrid laser-MIG welding of aluminum alloys: the influence of shielding gases, Appl. Surf. Sci. 255 (2009) 5588–5590, https://doi.org/10.1016/j.apsusc.2008.07.169.
[18] S.W. Campbell, A.M. Galloway, G.M. Ramsey, N.A. McPherson, A computational fluid dynamic analysis of the effect of weld nozzle geometry changes on shielding gas coverage during gas metal arc welding, J. Manuf. Sci. Eng. 135 (2013), https://doi.org/10.1115/1.4024817.
[19] G. Kickelbick, Chemie für Ingenieure, 2008.
[20] V. Chandola, A. Banerjee, V. Kumar, Anomaly detection, ACM Comput. Surv. 41 (2009) 1–58, https://doi.org/10.1145/1541880.1541882.
[21] Y. Ma, Z. Hu, Y. Tang, S. Ma, Y. Chu, X. Li, W. Luo, L. Guo, X. Zeng, Y. Lu, Laser opto-ultrasonic dual detection for simultaneous compositional, structural, and stress analyses for wire + arc additive manufacturing, Addit. Manuf. 31 (2020), 100956, https://doi.org/10.1016/j.addma.2019.100956.
[22] Y. Huang, F. Li, Y. Zhang, Y. Cai, X. Hua, Spectral analysis of the dynamic behavior of a welding arc during pulsed gas metal arc welding of AA5083 aluminum alloy with ER5183 wire, IEEE Trans. Plasma Sci. 47 (2019) 5078–5088, https://doi.org/10.1109/TPS.2019.2948205.
[23] Z. Zhao, Y. Guo, L. Bai, K. Wang, J. Han, Quality monitoring in wire-arc additive manufacturing based on cooperative awareness of spectrum and vision, Optik 181 (2019) 351–360, https://doi.org/10.1016/j.ijleo.2018.12.071.
[24] R. Reisch, T. Hauser, T. Kamps, A. Knoll, Robot based wire arc additive manufacturing system with context-sensitive multivariate monitoring framework, in: Proceedings of the 30th International Conference on Flexible Automation and Intelligent Manufacturing, Procedia Manufacturing 51, 2020, 732–739. https://doi.org/10.1016/j.promfg.2020.10.103.
[25] R. Reisch, T. Hauser, B. Lutz, M. Pantano, T. Kamps, A. Knoll, Distance-based multivariate anomaly detection in wire arc additive manufacturing, in: Proceedings of the IEEE International Conference on Machine Learning and Applications (ICMLA) 19, 2020, 659–664. https://doi.org/10.1109/ICMLA51294.2020.00109.
[26] Q. Miao, D. Wu, D. Chai, Y. Zhan, G. Bi, F. Niu, G. Ma, Comparative study of microstructure evaluation and mechanical properties of 4043 aluminum alloy fabricated by wire-based additive manufacturing, Mater. Des. 186 (2020), 108205, https://doi.org/10.1016/j.matdes.2019.108205.
[27] T. Hauser, P.P. Breese, T. Kamps, C. Heinze, J. Volpp, A.F.H. Kaplan, Material transitions within multi-material laser deposited intermetallic iron aluminides, Addit. Manuf. 34 (2020), 101242, https://doi.org/10.1016/j.addma.2020.101242.
[28] Y. Sugiyama, J. Nakata, H. Miyauchi, Reducing smut in aluminium alloy welds using double wire MIG (DWM) welding, Weld. Int. 7 (1993) 177–182, https://doi.org/10.1080/09507119309548369.